of the O_2 into the structure and CO_X products out of the bulk. Upon cooling, there is a phase change with 7% volume change in the cristobalite (*21*), as well as a large shift in coefficient of thermal expansion (*22*), which leads to a cracked surface oxide. Upon reheating, the oxidation appears to restart underneath the cracked oxide layer, leading to a multilayer oxide scale after several heat treatments. X-ray diffraction did not detect phases other than cristobalite, indicating that bulk crystallization products, specifically β-SiC, were not present or were below the detection limit due to their small size and volume fraction (fig. S3). TEM of a sample heat-treated for 10 hours at 1300°C followed by 10 hours at 1500°C revealed the onset of bulk crystallization with scattered β-SiC crystals <10 nm inside the amorphous matrix. A lamella was milled out of a fractured surface of a microlattice strut, as indicated by the rectangle in Fig. 4C, so that oxide and SiOC base material could be analyzed (Fig. 4D). Bright-field images showed small crystallites of a few nanometers in size in both the oxide and SiOC region. High-resolution imaging could identify the crystallites as graphite and β-SiC, based on the lattice spacing and diffraction pattern (Fig. 4E). The small size of 5 to 10 nm of the crystals and the high fraction of remaining amorphous matrix indicate that crystallization had just started. The crystallites in the silicon oxide region are even smaller (Fig. 4F), consistent with the recent formation of this oxide region. Larger crystals are probably present in older oxide layers further from the interface, contributing to the cristobalite diffraction pattern recorded by XRD below. Noteworthy were small pores in the SiOC region that were not observed before the heat treatments and presumably developed due to carbon leaving as CO or CO_2 gas.

This indicates that the amorphous $SiO_{1.34}C_{1.25}S_{0.15}$ is more stable than other silicon oxycarbide compositions, which crystallize sooner (*23*). The high-temperature stability with respect to mass change in air is compared with other materials in Fig. 4B (mass change was extrapolated from reported mass versus time curves after 1 hour exposure in air). The silicon-oxycarbide structures show better oxidation performance than silicon oxycarbide materials from previous studies, which used different starting precursors, compositions, and pyrolysis temperatures (*20*, *24*, *25*). Silicon oxycarbide is more resistant to oxidation than SiC and Si_3N_4 and has been investigated as oxidation protection coating for these materials (*8*).

Various ceramic compositions can be processed with our approach, including materials that are difficult to form via sintering of powders, such as SiOC, Si_3N_4, and SiC ceramics. In this demonstration, we focused on structures out of silicon oxycarbide, and our cellular SiOC materials exhibit strength 10 times as high as commercially available ceramic foams of similar density and survive temperatures of 1700°C in air with surface oxidation. Such cellular ceramic materials are of interest for the core of lightweight, load-bearing ceramic sandwich panels for high-temperature applications—for example, in hypersonic vehicles and jet engines. Stereolithography of ceramics will open opportunities for complex-shaped, temperature- and environment-resistant ceramic structures from the microscale—e.g., in microelectromechanical systems (MEMS) or device packaging—to the macro scale—e.g., in propulsion or thermal protection systems.

REFERENCES AND NOTES

1. J. Deckers, J. Vleugels, J.-P. Kruth, *J. Ceram. Sci. Technol.* **5**, 245–260 (2014).
2. N. Travitzky *et al.*, *Adv. Eng. Mater.* **16**, 729–754 (2014).
3. A. Zocca, P. Colombo, C. M. Gomes, J. Günster, *J. Am. Ceram. Soc.* **98**, 1983–2001 (2015).
4. T. T. Wohlers, T. Caffrey, *Wohlers Report* (Wohlers Associates, Fort Collins, CO, 2013).
5. P. Colombo, G. Mera, R. Riedel, G. D. Sorarù, *J. Am. Ceram. Soc.* **93**, 1805–1837 (2010).
6. S. Martínez-Crespiera *et al.*, *Sens. Actuators A Phys.* **169**, 242–249 (2011).
7. L.-A. Liew *et al.*, *Sens. Act. A* **95**, 120–134 (2002).
8. P. Colombo, R. Riedel, G. D. Sorarù, H. J. Kleebe, Eds., *Polymer Derived Ceramics* (DEStech Publications, Lancaster, PA, 2010).
9. M. Schulz *et al.*, *Adv. Eng. Mater.* **6**, 676–680 (2004).
10. A. J. Jacobsen, W. Barvosa-Carter, S. Nutt, *Adv. Mater.* **19**, 3892–3896 (2007).
11. T. A. Schaedler *et al.*, *Science* **334**, 962–965 (2011).
12. R. Riedel *et al.*, *Nature* **382**, 796–798 (1996).
13. M. Zaheer, T. Schmalz, G. Motz, R. Kempe, *Chem. Soc. Rev.* **41**, 5102–5116 (2012).
14. P. Colombo, J. R. Hellmann, D. L. Shelleman, *J. Am. Ceram. Soc.* **84**, 2245–2251 (2001).
15. L. J. Gibson, M. F. Ashby, *Cellular Solids: Structure and Properties* (Cambridge Univ. Press, Cambridge, 1997).
16. A. J. Jacobsen, W. Barvosa-Carter, S. Nutt, *Acta Mater.* **55**, 6724–6733 (2007).
17. A. J. Jacobsen, W. Barvosa-Carter, S. Nutt, *Acta Mater.* **56**, 2540–2548 (2008).
18. T. Varga *et al.*, *J. Am. Ceram. Soc.* **90**, 3213–3219 (2007).
19. A. Saha, R. Raj, D. L. Williamson, *J. Am. Ceram. Soc.* **89**, 2188–2195 (2006).
20. T. Xu, Q. Ma, Z. Chen, *Ceram. Int.* **37**, 2555–2559 (2011).
21. M. D. Beals, S. Zerfoss, *J. Am. Ceram. Soc.* **27**, 285–292 (1944).
22. L. Huang, J. Kieffer, *J. Chem. Phys.* **118**, 1487–1498 (2003).
23. A. Saha, R. Raj, *J. Am. Ceram. Soc.* **90**, 578–583 (2007).
24. S. Modena, G. D. Soraru, Y. Blum, R. Raj, *J. Am. Ceram. Soc.* **88**, 339–345 (2005).
25. G. Chollon, *J. Eur. Ceram. Soc.* **20**, 1959–1974 (2000).
26. W. C. Tripp, H. C. Graham, *J. Am. Ceram. Soc.* **59**, 399–403 (1976).
27. E. Opila, S. Levine, J. Lorincz, *J. Mater. Sci.* **39**, 5969–5977 (2004).
28. W. C. Tripp, H. C. Graham, *J. Electrochem. Soc.* **118**, 1195–1199 (1971).
29. J. A. Coppala, M. Srinivasan, K. T. Faber, R. H. Smoak (The Carborundum Company, USA)., in Proceedings of International Symposium on Factors in Densification and Sintering of Oxide and Non-oxide Ceramics, October 3 to 5, 1978, Hakone, Japan (Gakujutsu Bunken Fukyu-kai, Tokyo, 1979), pp. 400–417.
30. N. M. Geyer, Aeronautical Systems Division Technical Report 61-322, from the published Proceedings for the Materials Symposium, 13 to 15 September 1961, Phoenix, AZ.

ACKNOWLEDGMENTS

The authors gratefully acknowledge financial support by HRL Laboratories, LLC, and the Defense Advanced Research Projects Agency under the Materials with Controlled Microstructural Architecture program managed by J. Goldwasser (contract no. W91CRB-10-0305) and thank N. Verma (University of California, Santa Barbara) for TEM analysis and C. G. Levi and C. S. Roper for useful discussions. Patent applications have been filed under serial numbers 62/183580, 62/128410, and 62/092733 with the U.S. Patent and Trademark office.

SUPPLEMENTARY MATERIALS

www.sciencemag.org/content/351/6268/58/suppl/DC1
Materials and Methods
Figs. S1 to S4
Tables S1 to S3
References

18 August 2015; accepted 13 November 2015
10.1126/science.aad2688

BLACK HOLE PHYSICS

A radio jet from the optical and x-ray bright stellar tidal disruption flare ASASSN-14li

S. van Velzen,[1]* G. E. Anderson,[2,3] N. C. Stone,[4] M. Fraser,[5] T. Wevers,[6] B. D. Metzger,[4] P. G. Jonker,[6,7] A. J. van der Horst,[8] T. D. Staley,[2] A. J. Mendez,[1] J. C. A. Miller-Jones,[3] S. T. Hodgkin,[5] H. C. Campbell,[5] R. P. Fender[2]

The tidal disruption of a star by a supermassive black hole leads to a short-lived thermal flare. Despite extensive searches, radio follow-up observations of known thermal stellar tidal disruption flares (TDFs) have not yet produced a conclusive detection. We present a detection of variable radio emission from a thermal TDF, which we interpret as originating from a newly launched jet. The multiwavelength properties of the source present a natural analogy with accretion-state changes of stellar mass black holes, which suggests that all TDFs could be accompanied by a jet. In the rest frame of the TDF, our radio observations are an order of magnitude more sensitive than nearly all previous upper limits, explaining how these jets, if common, could thus far have escaped detection.

Although radio jets are a ubiquitous and well-studied feature of accreting compact objects, it remains unclear why only a subset of active galactic nuclei (AGNs) are radio-loud. A stellar tidal disruption flare (TDF) presents a novel method with which to study jet production in accreting supermassive black holes. These flares occur after perturbations to a star's orbit have brought it to within a few tens of Schwarzschild radii of the central supermassive black hole and the star gets torn apart by the black hole's tidal force. A large amount of gas is suddenly

injected close to the black hole event horizon, and we therefore anticipate the launch of a relativistic jet as this stellar debris gets accreted (*1*, *2*). About two dozen TDFs have so far been discovered at soft x-ray, ultraviolet (UV), and optical wavelengths (*3*–*5*). All of these flares can be described by black body emission, hence their description as thermal TDFs. Hard x-ray emission from a relativistic jet launched after a stellar disruption has been observed in three cases (*6*–*10*). These so-called relativistic TDFs are readily detected at radio frequencies [the best-studied source, Swift J1644+57, reached a peak flux of 30 millijansky (mJy) at 22 GHz (*11*, *12*)]. Surprisingly, radio observations of thermal TDFs show no signs of equally powerful jets (*13*, *14*), bringing into question the universality of jet production triggered by large changes in the accretion rate (*15*).

On 2 December 2014, the All-Sky Automated Survey for Supernovae (ASAS-SN) reported the discovery of ASASSN-14li (*16*), an optical transient with a blue continuum in Swift UV/Optical Telescope (UVOT) follow-up observations, located in the nucleus of a galaxy at redshift $z = 0.021$. These properties prompted this transient to be classified as a potential stellar tidal disruption flare. The source was also detected in Swift X-ray Telescope (XRT) observations, but only at soft x-ray energies (0.3 to 1 keV) (Fig. 1). We began a radio monitoring campaign with the Arcminute Microkelvin Imager (AMI) at 15.7 GHz 22 days after the first Swift observation and obtained two observations with the Westerbork Synthesis Radio Telescope (WSRT) at 1.4 GHz (supplementary text and table S1). The 15.7-GHz light curve shows a monotonic decay (factor 5 decrease in 140 days) (Fig. 2), suggesting that we observed the fading of a relativistic outflow that was produced by the impulsive accretion event onto the supermassive black hole.

The host galaxy is detected at 3 mJy in archival radio images at 1.4 GHz. The expected radio flux due to star formation is at most 10^{-3} mJy (supplementary text), and we therefore conclude that the preflare radio flux is due to an AGN. The only other property of the host that suggests ongoing accretion before the flare in 2014 is narrow [O III] line emission with a luminosity of $L_{[O III]} = 8 \times 10^{38}$ erg s^{-1}. This low luminosity implies that the AGN was in the radiatively inefficient, jet-dominated mode (*17*).

On the basis of the detection of an AGN before the optical flare, one might infer ASASSN-14li to be a brief period of enhanced activity of the pre-existing accretion disk, but this is inconsistent with nearly all of the observed properties of the flare. First, the very low x-ray black body temperature ($T \approx 0.06$ keV), including substantial absorption features, is unlike the x-ray properties of any known AGN (*18*). Second, the large x-ray flux increase with respect to the archival upper limit (Fig. 1) is seen for less than 0.5% of sources in a blind all-sky search for x-ray variability (*19*). Third, the factor of 100 increase with respect to the baseline UV flux seen in ASASSN-14li is more than an order of magnitude larger than observed in a 3-year monitoring campaign of 663 AGN (*20*). And last, we found no significant variability in 8 years of optical observations of the host galaxy of ASASSN-14li by the Catalina Real-Time Transient Survey. A stellar tidal disruption is therefore the best interpretation for ASASSN-14li.

The x-ray temperature and luminosity of ASASSN-14li are similar to thermal TDFs discovered with x-ray surveys (*3*) and can be explained by a newly formed, radiatively efficient accretion disk with an inner radius at a few Schwarzschild radii from the black hole (*21*). Its optical/UV properties are also very similar to previous optically discovered TDFs, which are characterized by a large and constant black body temperature [$T = (2 - 3) \times 10^4$ K] (table S5 and fig. S2).

Thermal TDFs are typically detected at optical/UV or soft x-ray frequencies, but not both (table S3). This could be explained by the existence of a region at 1000 Schwarzschild radii from the black hole that produces the optical emission via reprocessing of the x-ray photons that originate from the inner accretion disk (*22*). If the product of the optical depth for x-ray ionization and the covering factor of this region is $\gg 1$, luminous optical emission would be produced while x-rays from the inner disk are obscured. In this model, ASASSN-14li can be explained if the evolution of the reprocessing layer gradually allows the escape of more x-ray photons toward our line of sight. This would explain why the x-ray light curve tracks the theoretical $t^{-5/3}$ fallback rate only after about 100 days into the monitoring campaign (Fig. 2) and why the optical light curve of x-ray dim TDFs show less variability than that of ASASSN-14li [for example, the x-ray dim TDF PS1-10jh (*23*) showed only 0.03 magnitude (mag) root-mean-square variability, compared with 0.2 mag for ASASSN-14li]. An alternative explanation for the initially constant x-ray flux is inefficient circularization of the tidal debris streams (*24*), which slows down the formation of the inner accretion disk.

The key property of ASASSN-14li is the detection of variable radio emission. Adopting the standard flat or slightly inverted radio spectrum (*17*) for emission of the original AGN jet, we found that our 15.7 GHz observations were always below the 3 mJy baseline level of this jet. The decaying 15.7 GHz light curve of ASASSN-14li therefore indicates that we have observed the termination of an AGN jet because of an increased accretion rate. If the AGN jet had not been terminated, we would have expected an increase with respect to this baseline level. Without an engine to drive particle acceleration in the AGN jet, the synchrotron luminosity will decrease on a time scale of ~10 days at 10 GHz. Inverse Compton cooling of the electrons on TDF photons can speed up this decrease by a factor ~10 (supplementary text). Hence, the radio flux of the original AGN jet is unlikely to be a dominant component to our post-flare radio observations.

The combined optical and x-ray luminosity during the first month of observations of ASASSN-14li

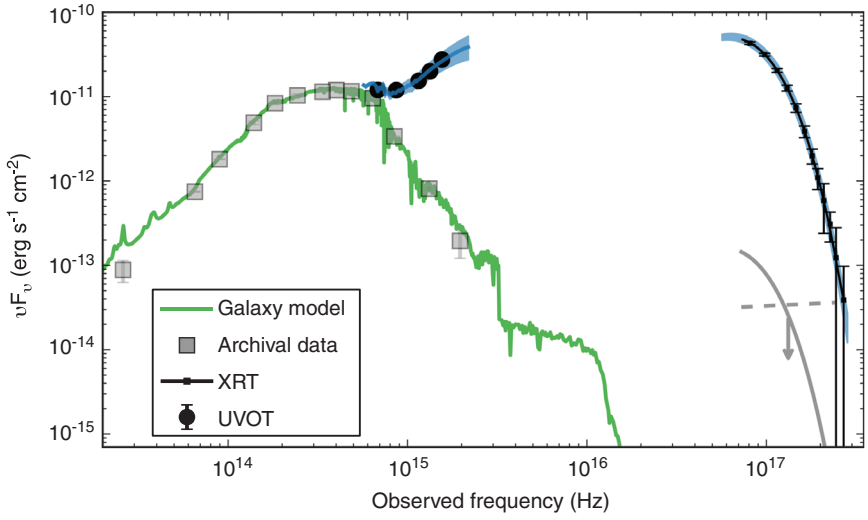

Fig. 1. Flare and host spectral energy distribution (SED). Shown is the first epoch of the series of Swift x-ray (unfolded spectrum) and broadband optical/UV observations of ASASSN-14li. These observations can each be described by a single black body with $T = 7.7 \times 10^5$ K and $T = 3.5 \times 10^4$ K, respectively (blue lines; width reflects uncertainty on the temperature). The SED of the host galaxy based on archival data (gray squares) shows no sign of star formation or an AGN as demonstrated by our best-fit synthetic galaxy spectrum (green line). The pre-flare x-ray limit is shown for both a black body spectrum of similar temperature as the current x-ray spectrum (gray solid line) and a standard power-law AGN spectrum ($\Gamma = 1.9$; gray dashed line).

[1]Department of Physics and Astronomy, The Johns Hopkins University, Baltimore, MD 21218, USA. [2]Department of Physics, University of Oxford, Denys Wilkinson Building, Keble Road, Oxford OX1 3RH, UK. [3]International Centre for Radio Astronomy Research, Curtin University, GPO Box U1987, Perth WA 6845, Australia. [4]Columbia Astrophysics Laboratory, Columbia University, New York, NY 10027, USA. [5]Institute of Astronomy, University of Cambridge, Madingley Road, Cambridge CB3 0HA, UK. [6]Department of Astrophysics, Radboud University Nijmegen, Heyendaalseweg 135, 6525 AJ Nijmegen, Netherlands. [7]SRON, Netherlands Institute for Space Research, Sorbonnelaan 2, 3584 CA Utrecht, Netherlands. [8]Department of Physics, The George Washington University, 725 21st Street NW, Washington, DC 20052, USA.
***Corresponding author. E-mail: sjoert@jhu.edu**

amounts to a few tens of percent of the Eddington luminosity [adopting a central black hole mass of $10^{6.5}$ solar mass ($M_\odot$)] (supplementary text), compared with <1% of the Eddington limit before the flare. ASASSN-14li shares several properties with the flares produced by stellar mass black holes upon being subjected to similarly large changes in their accretion rates. Accretion onto stellar mass black holes in x-ray binaries (XRBs) occurs in two distinct spectral modes, which are separated by a state change that occurs at a few percent of the Eddington luminosity (*25*). Radio observations of XRBs consistently show the disappearance of a steady compact jet and the launch of transient ejecta during the change from the nonthermal (hard) state to the thermal (soft) state (*15*). In direct analogy with XRBs, the steady jet that existed before the infall of material from the tidal disruption has been quenched or suppressed, and the accretion disk spectrum is now dominated by thermal emission. The co-added Swift XRT data of the TDF shows no evidence for a nonthermal (2 to 10 keV) component at the level needed to power the preflare [OIII] line luminosity (supplementary text), suggesting that the geometrically thick accretion flow that powered the previous steady jet has collapsed.

The maximum radio luminosity of ASASSN-14li is three orders of magnitude lower than that of Swift J1644+57 (*11*) and evolves on a much shorter time scale. This immediately implies a large difference in jet power between these two events. The radio light curve of ASASSN-14li can be reproduced by using a model similar to that applied to Swift J1644+57 (*1*), in which synchrotron shock emission is produced as the transient ejecta decelerate upon interacting with dense gas in the nuclear region surrounding the black hole. Assuming the ejecta were launched ~20 days before the first Swift observation of ASASSN-14li and applying a simple blast wave model yields a total jet energy of $E_j \sim 10^{48}$ erg, under the common assumption that 20 and 1% of the energy dissipated by the shocks is placed into relativistic electrons and magnetic fields, respectively (*1*). This energy is four orders of magnitude lower than the total jet energy of Swift J1644+57 (*26*).

By the time of our radio observations, the newly launched jet would have swept up enough matter to slow to mildly relativistic velocities (bulk Lorentz factor $\Gamma_j \approx 2$), causing each lobe to spread laterally in a quasispherical manner (similar to a mushroom cloud). The approximately isotropic nature of the radio emission at the time of the observations also implies that a finely tuned viewing angle with respect to the jet axis is not required. The gas density of ~10^3 cm^{-3} that is required to decelerate the jet at a characteristic radius of 0.1 pc can be explained by the Bondi accretion flow needed to supply the radiatively inefficient flow that existed before the flare (supplementary text). The deceleration of the new jet implies it cannot be launched into the funnel cleared by the previous jet, which occurs naturally if the new jet orientation is determined by the angular momentum of the new accretion disk rather than the black hole spin vector.

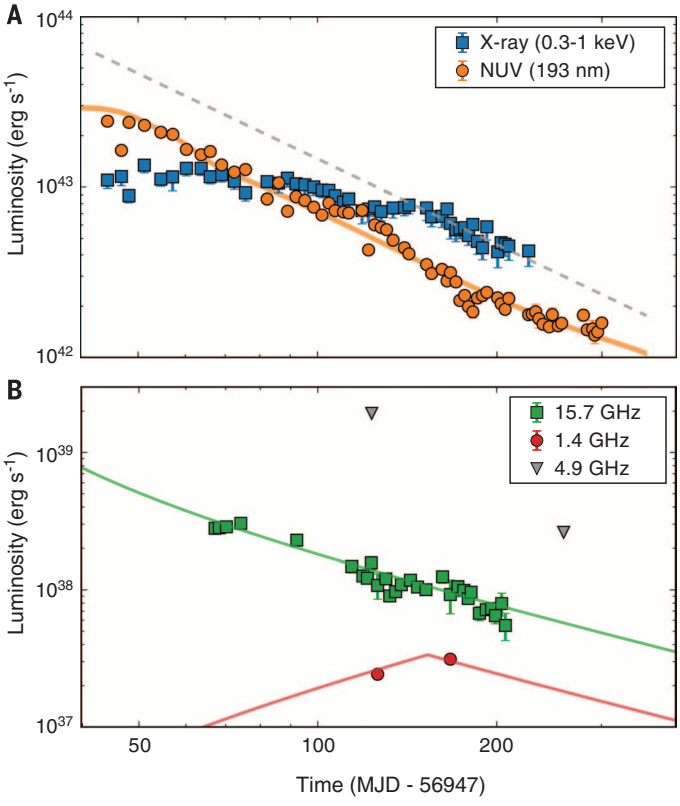

Fig. 2. Multi-wavelength light curves of the tidal disruption flare ASASSN-14li. (**A**) Integrated soft x-ray (0.3 to 1 keV) luminosity and monochromatic (νL_ν) near-UV (UVW2-band) luminosity. A spline fit to the observed *g*-band light curve of the known tidal flare PS1-10jh (*23*), corrected for cosmological time dilation and scaled up by 15%, is shown for reference (solid line). The dashed gray line indicates a $(t - t_0)^{-5/3}$ power law, the approximate theoretically expected fallback rate of the stellar debris for a disruption at t_0. The normalization of the time axis [in Modified Julian Day (MJD)] is chosen to highlight that the (late-time) light curves are consistent with this power law (t_0 = 56947 ± 2 MJD) (fig. S1). Error bars show the 1σ statistical uncertainty, often smaller than the marker size. (**B**) Monochromatic radio luminosity at 15.7 GHz (AMI) and 1.4 GHz (WSRT) of ASASSN-14li and our jet model (solid lines). The spectral indices during the two epochs of dual radio frequency coverage are −0.4 ± 0.1 and −0.6 ± 0.1 (first and second epoch, respectively). The two most stringent upper limits on the early-time 5-GHz emission of previous thermal TDFs (gray triangles) (table S4) were not sensitive enough to detect transient radio emission similar to ASASSN-14li.

Adopting the analogy of tidal disruption events as laboratories for studying accretion physics, we have thus far obtained two well-sampled multiwavelength experiments with very different outcomes: One yielded a powerful jet (Swift J1644+57), whereas the second event—promptly followed up at radio frequencies (ASASSN-14li)—revealed a much weaker jet. A common explanation for the wide range of black hole jet efficiency is black hole spin—powerful jets require higher spin. This model, however, cannot readily explain the radio light curve of ASASSN-14li because it would predict that the radio luminosity should increase after the disruption (because the spin remains unchanged, whereas the gas supply is greatly enhanced with respect to the predisruption accretion rate). Besides spin, powerful jets may require a large magnetic flux near the black hole horizon (*27*). Our observations could suggest that the magnetic flux stored in a preexisting accretion flow is not tapped efficiently upon the disruption and accretion of a star, contrary to simulation predictions (*28*).

The majority of radio follow-up observations of thermal TDFs were obtained many years after the peak of the flare. Our observations are the first to sample the light curve within 30 days of the peak. Combined with the low redshift of ASASSN-14li, this explains why similar jets in previous thermal TDFs have eluded detection (table S4). In analogy with the consistent production of transient jets during accretion flow state changes of stellar mass black holes, our observations suggest that radio-emitting outflows could be a common feature of all TDFs. Adopting a 5σ detection threshold of 90 μJy for a monthly all-sky survey with the Square Kilometer Array at 1.4 GHz (*29*), a galaxy density of 5×10^{-3} Mpc^{-3} and a jet production rate equal to the observed thermal TDF rate [3×10^{-5} galaxy^{-1} year^{-1} (*30*)] yields a detection rate of ~10^2 thermal TDF jets per year. Although the nonthermal tidal disruption jets selected by Swift are much more powerful, they are a smaller subpopulation of all stellar disruptions. In blind radio transients surveys, both types of TDF jets could be detected at roughly similar rates.

REFERENCES AND NOTES

1. D. Giannios, B. D. Metzger, *Mon. Not. R. Astron. Soc.* **416**, 2102–2107 (2011).
2. S. van Velzen, E. Körding, H. Falcke, *Mon. Not. R. Astron. Soc.* **417**, L51–L55 (2011).
3. N. Bade, S. Komossa, M. Dahlem, *Astron. Astrophys.* **309**, L35 (1996).
4. S. Gezari *et al.*, *Astrophys. J.* **698**, 1367–1379 (2009).
5. S. van Velzen *et al.*, *Astrophys. J.* **741**, 73 (2011).
6. J. S. Bloom *et al.*, *Science* **333**, 203–206 (2011).
7. A. J. Levan *et al.*, *Science* **333**, 199–202 (2011).
8. D. N. Burrows *et al.*, *Nature* **476**, 421–424 (2011).
9. S. B. Cenko *et al.*, *Astrophys. J.* **753**, 77 (2012).
10. G. C. Brown *et al.*, *Mon. Not. R. Astron. Soc.* **452**, 4297–4306 (2015).
11. B. A. Zauderer *et al.*, *Nature* **476**, 425–428 (2011).
12. E. Berger *et al.*, *Astrophys. J.* **748**, 36 (2012).
13. G. C. Bower, B. D. Metzger, S. B. Cenko, J. M. Silverman, J. S. Bloom, *Astrophys. J.* **763**, 84 (2013).
14. S. van Velzen, D. A. Frail, E. Körding, H. Falcke, *Astron. Astrophys.* **552**, A5 (2013).
15. R. P. Fender, T. M. Belloni, E. Gallo, *Mon. Not. R. Astron. Soc.* **355**, 1105–1118 (2004).
16. T. W.-S. Holoien *et al.*, *Mon. Not. R. Astron. Soc.*; http://arxiv.org/abs/1507.01598 (2015).
17. H. Falcke, E. Körding, S. Markoff, *Astron. Astrophys.* **414**, 895 (2004).
18. J. M. Miller *et al.*, *Nature* **526**, 542–545 (2015).
19. J. Kanner *et al.*, *Astrophys. J.* **774**, 63 (2013).
20. S. Gezari *et al.*, *Astrophys. J.* **766**, 60 (2013).
21. A. Ulmer, *Astrophys. J.* **514**, 180–187 (1999).
22. J. Guillochon, H. Manukian, E. Ramirez-Ruiz, *Astrophys. J.* **783**, 23 (2014).
23. S. Gezari *et al.*, *Nature* **485**, 217–220 (2012).
24. H. Shiokawa, J. H. Krolik, R. M. Cheng, T. Piran, S. C. Noble, *Astrophys. J.* **804**, 85 (2015).
25. T. J. Maccarone, *Astron. Astrophys.* **409**, 697–706 (2003).
26. P. Mimica, D. Giannios, B. D. Metzger, M. A. Aloy, *Mon. Not. R. Astron. Soc.* **450**, 2824–2841 (2015).
27. J. C. McKinney, A. Tchekhovskoy, R. D. Blandford, *Science* **339**, 49–52 (2013).
28. L. Z. Kelley, A. Tchekhovskoy, R. Narayan, *Mon. Not. R. Astron. Soc.* **445**, 3919–3938 (2014).
29. R. Fender *et al.*, in *Advancing Astrophysics with the Square Kilometre Array*, T. L. Bourke *et al.*, Eds. (Proceedings of Science, 2014), chap. 51.
30. S. van Velzen, G. R. Farrar, *Astrophys. J.* **792**, 53 (2014).

ACKNOWLEDGMENTS

We are grateful to the ASAS-SN team for making their newly identified optical transient public. We thank J. Krolik for useful discussions. We thank the staff of the Mullard Radio Astronomy Observatory for their invaluable assistance in the operation of AMI. We thank the WSRT director for granting the observations in Director's Discretionary Time and the WSRT staff for obtaining these observations. The WSRT is operated by ASTRON (Netherlands Institute for Radio Astronomy) with support from the Netherlands foundation for Scientific Research. S.v.V. is supported by NASA through a Hubble Fellowship (HST-HF2-51350.001). G.E.A., T.D.S., and R.P.F. acknowledge support from the European Research Council via Advanced Investigator Grant 267697. G.E.A. also acknowledges the support of the International Centre for Radio Astronomy Research (ICRAR), a Joint Venture of Curtin University and The University of Western Australia, funded by the Western Australian State government. M.F. and H.C.C. acknowledge support from the European Union FP7 program through European Research Council grant 320360. B.D.M. and N.C.S. acknowledge support from NASA grant NNX14AQ68G, NSF grant AST-1410950, and the Alfred P. Sloan Foundation. N.C.S. is also supported by NASA through an Einstein Fellowship. J.C.A.M.-J. is supported by an Australian Research Council Future Fellowship (FT140101082). The data presented here can be found in the supplementary materials; raw optical/UV/x-ray observations are available in the NASA/Swift archive (http://heasarc.nasa.gov/docs/swift/archive, Target Name: BRUTUS6984_2); raw radio observations (WSRT and AMI) are maintained by the observatories and available upon request.

SUPPLEMENTARY MATERIALS

www.sciencemag.org/content/351/6268/62/suppl/DC1
Supplementary Text
Figs. S1 and S2
Tables S1 to S5
References (*31*–*106*)

31 July 2015; accepted 13 November 2015
Published online 26 November 2015
10.1126/science.aad1182

ASTROCHEMISTRY

Statistical ortho-to-para ratio of water desorbed from ice at 10 kelvin

Tetsuya Hama,* Akira Kouchi, Naoki Watanabe

The anomalously low ortho-to-para ratios (OPRs) exhibited by gaseous water in space have been used to determine the formation temperature (< 50 kelvin) of ice on cold interstellar dust. This approach assumes that the OPR of water desorbed from ice is related to the ice formation temperature on the dust. However, we report that water desorbed from ice at 10 kelvin shows a statistical high-temperature OPR of 3, even when the ice is produced in situ by hydrogenation of O_2, a known formation process of interstellar water. This invalidates the assumed relation between OPR and temperature. The necessary reinterpretation of the low OPRs will help elucidate the chemical history of interstellar water from molecular clouds and processes in the early solar system, including comet formation.

Astronomical observations have revealed water (H_2O) to be ubiquitous in space. Gaseous H_2O has been discovered in star- and planet-forming regions and in the atmospheres of planets both in and beyond our solar system. H_2O ice is also abundant in cold interstellar clouds and solar-system bodies such as comets. Studying the chemistry of the H_2O in these sources can provide information about their physical conditions and eventually may help us to understand the evolution of stars and planetary systems, including our solar system (*1*–*3*). Spectroscopy can reveal the abundance ratio of nuclear spin isomers of H_2O, namely the ortho-to-para ratio (OPR). Because a proton is a fermion with a nuclear spin angular momentum of $I = {}^1/_2$, two nuclear spin isomers exist for H_2O: ortho (I = 1, triplet) and para (I = 0, singlet). Conversion between the nuclear spin isomers by radiation or nonreactive collisions is extremely slow in the gas phase (*4*, *5*). The different nuclear spin isomers are thus treated as almost entirely separate species, making the OPR a valuable tracer for the physical and chemical history experienced by molecules, including their formation (*1*). The OPR is related to the spin temperature (T_{spin}) by Eq. 1, which is defined at thermodynamic equilibrium (*6*)

$$\mathrm{OPR} = \frac{3\sum(2J+1)\exp\left[\frac{-E_o(J_{K_a,K_c})}{k_B T_{spin}}\right]}{\sum(2J+1)\exp\left[\frac{-E_p(J_{K_a,K_c})}{k_B T_{spin}}\right]} \quad (1)$$

where $E_o(J_{K_a,K_c})$ and $E_p(J_{K_a,K_c})$ are the energy of a rotational level in ortho- and para-H_2O, respectively, and k_B is the Boltzmann constant. J is the

Institute of Low Temperature Science, Hokkaido University, Sapporo 060–0819, Japan.
*Corresponding author. E-mail: hama@lowtem.hokudai.ac.jp

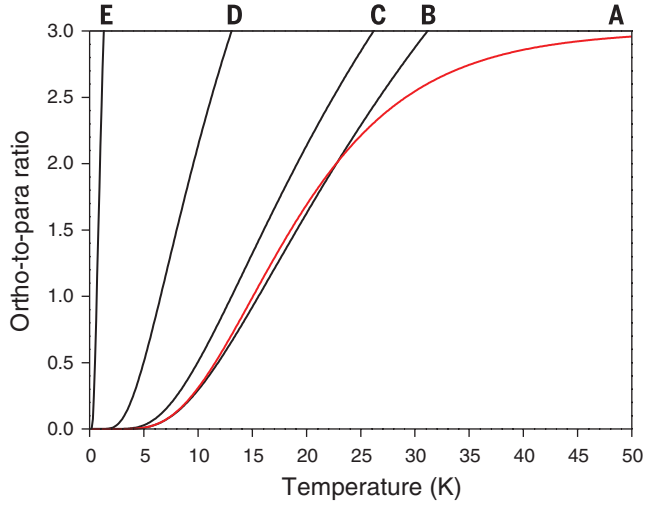

Fig. 1. OPR of H_2O as function of temperature. Curve A is calculated from Eq. 1 with the gas-phase constants (*7*). Approximated curves B to E are calculated from Eq. 9 with ΔE values of (B) 23.8 cm^{-1} (gas-phase), (C) 20 cm^{-1} (H_2O in Ar matrix) (*22*), (D) 10 cm^{-1}, and (E) 1.0 cm^{-1}. Approximated curves B to E tend toward 9, not the statistical OPR value of 3, because only the lowest ortho- and para-rotational states are considered in Eq. 9, and thus the contribution of the rotational degeneracy is not cancelled as in curve A from Eq. 1.

A radio jet from the optical and x-ray bright stellar tidal disruption flare ASASSN-14li

S. van Velzen, G. E. Anderson, N. C. Stone, M. Fraser, T. Wevers, B. D. Metzger, P. G. Jonker, A. J. van der Horst, T. D. Staley, A. J. Mendez, J. C. A. Miller-Jones, S. T. Hodgkin, H. C. Campbell and R. P. Fender

Science **351** (6268), 62-65.
DOI: 10.1126/science.aad1182originally published online November 26, 2015

Transient radio jet from a black hole

When a star passes too close to a supermassive black hole, it gets ripped apart by the gravitational forces. This causes a tidal disruption flare as the material falls into the black hole. van Velzen *et al.* monitored one such flare with radio telescopes and found evidence for a transient relativistic jet launched by the black hole (see the Perspective by Bower). Larger jets are a feature of active galactic nuclei and have a profound effect on their host galaxy, but are poorly understood. The results will aid our understanding of how black holes "feed" and of the processes governing jet formation.

Science, this issue p. 62; see also p. 30